Hindawi
International Journal of Photoenergy
Volume 2024, Article ID 8859153, 17 pages
https://doi.org/10.1155/2024/8859153

Research Article

Enhancing $CsSn_{0.5}Ge_{0.5}I_3$ Perovskite Solar Cell Performance via Cu_2O Hole Transport Layer Integration

Abu Rayhan, M. A. Khan, and Md. Rabiul Islam

Department of Electrical and Electronic Engineering, Bangabandhu Sheikh Mujibur Rahman Science and Technology University, Gopalganj 8100, Bangladesh

Correspondence should be addressed to M. A. Khan; asad.khan@bsmrstu.edu.bd

Received 18 May 2023; Revised 6 March 2024; Accepted 25 March 2024; Published 30 April 2024

Academic Editor: Daniel T. Cotfas

Copyright © 2024 Abu Rayhan et al. This is an open access article distributed under the Creative Commons Attribution License, which permits unrestricted use, distribution, and reproduction in any medium, provided the original work is properly cited.

Perovskite solar cells (PSCs) have emerged as a promising alternative to traditional silicon solar cells due to their low cost of fabrication and high power conversion efficiency (PCE). The utilization of lead halide perovskites as absorber layers in perovskite solar cells has been impeded by two major issues: lead poisoning and stability concerns. These hindrances have greatly impeded the industrialization of this cutting-edge technology. In light of the harmful effects of lead in perovskite solar cells, researchers have shifted their attention to exploring lead-free metal halide perovskites. However, the present alternatives to lead-based perovskite exhibit poor performance, thus prompting further inquiry into this matter. The primary objective of this research is to investigate the use of Cu_2O as a hole transport layer in combination with lead-free metal halide perovskite ($CsSn_{0.5}Ge_{0.5}I_3$) to achieve superior performance. Through meticulous experimentation, the suggested model has achieved outstanding results by optimizing several key variables. These variables include the thickness of the absorber layer ($CsSn_{0.5}Ge_{0.5}I_3$), defect density, and doping densities, as well as the back contact work function and the operating temperature associated with each layer. The proposed FTO/$PC_{60}BM$/$CsSn_{0.5}Ge_{0.5}I_3$/Cu_2O/Au solar cell structure surpassed prior configurations by comprehensively examining key aspects such as absorber layer thickness and defect density, doping densities, and back contact work. The structure has been also compared with multiple electron transport elements and concluded that the proposed model functions superior due to the use of $PC_{60}BM$ as an electron transport layer and it has an improved electron extraction procedure. Finally, the proposed model has achieved the optimized values as J_{sc} of 31.56 mA/cm^{-2}, V_{oc} of 1.12 V, FF of 81.47%, and PCE of 27.72%. As a consequence of this research, the investigated structure may be an excellent contender for the eventual creation of lead-free solar power cells made from perovskite.

1. Introduction

The field of photovoltaic cells has experienced a notable increase in the utilization of hybrid perovskite, which has arisen as a substantial asset within the industry. Chalcogenide perovskites, particularly $BaZrS_3$, have recently gained attention as reliable and environmentally friendly alternatives for various energy conversion applications, addressing issues associated with halide perovskites. Thakur et al. investigate the $BaZrS_3$ synthesis methods, highlight its unique properties, and discuss current challenges and future trends in the field [1–3]. Hybrid perovskite's cost-effectiveness has driven its burgeoning use in photovoltaic cells. The photovoltaic energy conversion efficiency of perovskite solar cells has increased profoundly [4]. This noteworthy accomplishment is a tribute to this industry's enormous progress and technological improvements [5–7]. Nevertheless, the prospects of photovoltaic perovskite cells are circumscribed by the perils of lead toxicity and durability [8]. To address the aforementioned challenges associated with lead in halogenated perovskites, various alternatives to Pb(II) have been proposed. These substitutes include silver (Ag(I)), germanium (Ge(II)), and tin (Sn(II)). Sn(II) halide perovskites have the most potential of all of these options. However, Tin (Sn(II)) soon oxidizes to tin (Sn(IV)), and the $CsSnI_3$ perovskite exhibits phase unpredictability, resulting in a loss of properties [9–11]. While oxidation can lead to performance degradation in some cases, in this architecture, the

oxidized Sn(IV) at the interface between the perovskite layer and the Cu_2O hole transport layer (HTL) might function as a passivating layer. This could mitigate charge recombination and enhance device stability [12]. $CsSn_{0.5}Ge_{0.5}I_3$ is a lead-free perovskite material with a strong potential for usage in solar cells [13]. It possesses a 1.5 eV bandgap, making it suitable for absorbing sunlight and turning it into energy [14]. $CsSn_{0.5}Ge_{0.5}I_3$ is also more stable in air and moisture than lead-based perovskites, making it a more appealing alternative [15].

The selection of the FTO/$PC_{60}BM$/$CsSn_{0.5}Ge_{0.5}I_3$/Cu_2O/Au solar cell configuration for this research paper was based on meticulous consideration of multiple factors. Firstly, the choice of FTO (fluorine-doped tin oxide) as the transparent conducting oxide (TCO) layer stems from its prevalent usage in solar cell research due to its exceptional electrical conductivity and transparency [16]. FTO enables the efficient collection and transport of photogenerated charges [17]. In the active layer, $PC_{60}BM$ (phenyl-C61-butyric acid methyl ester) was chosen as the electron acceptor material due to its well-established compatibility with perovskite-based solar cells [18]. $PC_{60}BM$ is widely employed as an acceptor due to its commendable electron-transporting properties, high electron mobility, and overall high efficiency as shown in Figure 1. Studies have consistently demonstrated the superior electron mobility and charge transport properties of $PC_{60}BM$ compared to $PC_{61}BM$ and PCBM, making it a preferred acceptor material in this photovoltaic model [19]. The carefully crafted molecular structure of $PC_{60}BM$, known for its specific phenyl-C61-butyric acid methyl ester arrangement, allows for better compatibility with donor materials. This unique feature results in improved device efficiency and stability compared to $PC_{61}BM$ and other forms of PCBM [20]. The primary focus of this study was on $CsSn_{0.5}Ge_{0.5}I_3$, a perovskite material that has demonstrated significant efficiency potential in previous investigations [13, 21]. By incorporating cesium (Cs), tin (Sn), and germanium (Ge) into the perovskite composition, it is expected to exhibit improved optoelectronic properties and enhanced stability compared to other perovskite materials [22]. The inclusion of a Cu_2O (cuprous oxide) layer serves as a hole transport layer (HTL) within the device architecture. Cu_2O is a promising material for hole extraction owing to its suitable energy levels and favorable hole mobility [23]. It facilitates efficient charge transport while minimizing charge recombination at the interface between the perovskite and electrode layers. For the top contact, an Au (gold) electrode was employed, following the conventional practice in solar cell designs. The utilization of Au is justified by its excellent electrical conductivity and stability [24]. The Au electrode enables the efficient collection of photogenerated holes and maintains low contact resistance. The chosen FTO/$PC_{60}BM$/$CsSn_{0.5}Ge_{0.5}I_3$/Cu_2O/Au configuration was thoughtfully selected to optimize charge collection, minimize recombination losses, and enhance the overall performance and stability of the perovskite solar cell device. Hybrid perovskite has revolutionized solar cell technology, but its limitations have led to the exploration of alternative materials. Perovskites containing both Ge and Sn show great promise for future applications. Wang et al. investigated the effects of adding germanium (Ge) to a type of perovskite material called $FA_{0.75}MA_{0.25}SnI_3$. This addition of Ge resulted in significant improvements in the performance of the material [25]. The researchers found that the Ge atoms were positioned on the surface of the perovskite and effectively addressed traps and imperfections present in the material. By doping $FA_{0.75}MA_{0.25}SnI_3$ with just 5% Ge, the photovoltaic conversion capability (PCE) of the material increased to 4.48%. Further research by the same authors explored the impact of doping $FA_{0.75}MA_{0.25}Sn_{0.95}Ge_{0.05}I_3$ with 5% Ge, which led to an even higher PCE of 7.9% [26]. In addition, Chen developed a different material called $CsSn_{0.5}Ge_{0.5}I_3$, demonstrating significant efficiency potential with a notable conversion efficiency of 7.11% [27]. In this material, Ge(II) ions were used to substitute Sn(II) cations, resulting in a decrease in the number of vacant positions within the material. This change played a crucial role in enhancing the overall performance of $CsSn_{0.5}Ge_{0.5}I_3$ [28]. To fully maximize the functionality of $CsSn_{0.5}Ge_{0.5}I_3$-based technologies, it is essential to gain a comprehensive understanding of the interaction between substance characteristics and device architecture [29]. By thoroughly exploring and comprehending the interactions between these variables, it will be possible to further enhance the operational efficiency of perovskite-based solar cells. This research opens up new avenues for improving the efficiency of solar energy conversion and brings us closer to developing more efficient and sustainable solar power technologies.

On the other hand, there have been a few steps in the model ($CsSn_{0.5}Ge_{0.5}I_3$-based perovskites) to prevent cesium toxicity. First, a decrement in the material's cesium concentration is needed [30]. By including a dopant in the substance, cesium toxicity can also be decreased [31]. Atoms called dopants are introduced to a semiconductor to alter its characteristics. Lithium (Li) is a suitable dopant for $CsSn_{0.5}Ge_{0.5}I_3$ [32]. Li does not occupy the same lattice positions as Cs and does not produce the same kind of poisoning since it has a smaller ionic radius [32]. Several steps may be taken to try to salvage the material if our $CsSn_{0.5}Ge_{0.5}I_3$-based perovskites have been contaminated by cesium. One is to raise the material's temperature significantly [33]. The cesium atoms may be forced out as a result. A chemical that can bond to cesium atoms can also be used to treat the substance. This may lessen the likelihood that the substance may be harmed by cesium atoms. Alloys encompassing germanium (Ge) and tin (Sn) show tremendous promise as materials for optoelectronic applications, owing to their worthwhile energy gap [34]. In addition, they have a higher resilience than conventional Sn-based perovskites. The suggested research considered optimizing approaches for perovskite solar cells leveraging an FTO/$PC_{60}BM$/$CsSn_{0.5}Ge_{0.5}I_3$/Cu_2O/Au setup and SCAPS-1D software, as shown in Figure 2. In the above arrangement, $PC_{60}BM$ acts like the electron-transporting layer (ETL), while Cu_2O functions as the hole transporter layer (HTL). This approach was picked since alloys encompassing germanium (Ge) and tin (Sn) have advantageous energy gap attributes, making them fascinating candidates for applications in optics [13]. Moreover, alloys like this are known to be more durable than pure Sn-based perovskites [35, 36].

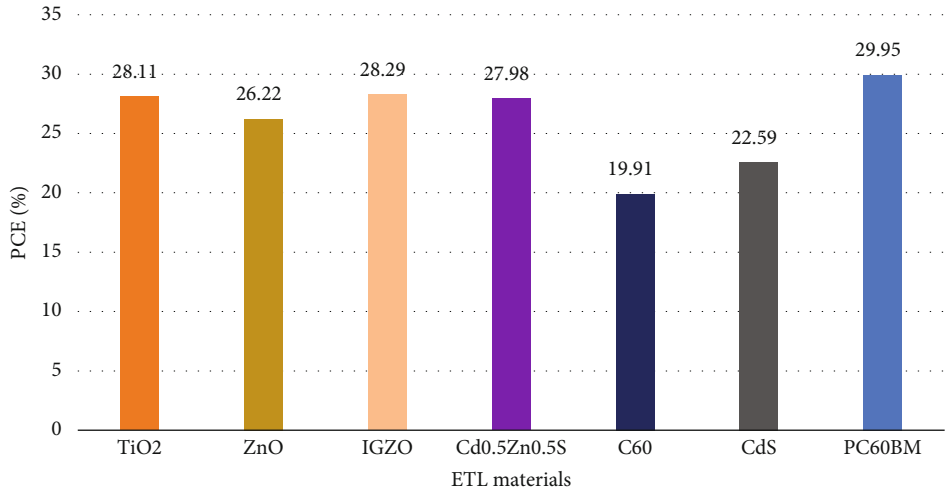

Figure 1: For each electron transport material employed, the PCE of the perovskite solar cell is calculated and $PC_{60}BM$ shows the highest efficiency.

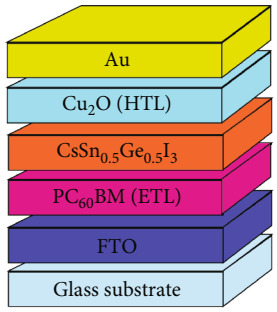

Figure 2: The proposed FTO/$PC_{60}BM$/$CsSn_{0.5}Ge_{0.5}I_3$/Cu_2O/Au solar cell configuration.

The tuning of perovskite solar cells was carried out by assessing variations in the cell's attributes in conjunction with a broad range of scenarios. The influence of the contributor density of $PC_{60}BM$ (electron transport layer) and recipient density of Cu_2O (hole transport layer), as well as the degree of thickness and number of defects of the $CsSn_{0.5}Ge_{0.5}I_3$ perovskite layer, variation in temperature, on the device's overall efficiency has been conducted. Overall, this research sheds illumination on the design and improvement of perovskite solar cells for enhanced effectiveness and performance.

2. Device Structure and Computational Modeling

The device structure of FTO/$PC_{60}BM$/$CsSn_{0.5}Ge_{0.5}I_3$/Cu_2O/Au has been shown in Figure 2. Table 1 lists the significant variables employed for simulating the noninverted planar architecture of photovoltaic cells composed of FTO/$PC_{60}BM$/$CsSn_{0.5}Ge_{0.5}I_3$/Cu_2O/Au. The simulations have been conducted at a working temperature of 300 Kelvin, accompanied by the customary AM1.5G spectrum as the illuminating source. A total number of simulations have been carried out, and these have been performed with a series resistor of 3.2 Ω and a shunt resistor of 3200 Ω. The SCAPS-1D program has been used to acquire data points from the devices and substances employed for the simulation.

The data shown in Table 1 have been chosen for the best performance on the proposed model. Some of the numbers listed are based on data obtained from the experiments [27, 37–40], and their arrangement takes into consideration varying several variables such as local weather, work function, and temperature.

3. Effect of Different HTL (Hole Transport Layer) with the $CsSn_{0.5}Ge_{0.5}I_3$ Perovskite Absorber Layer

3.1. Energy Band Alignment Diagram and Energy Band Diagram of Different Hole Transport Layers. The band alignment diagram of different hole transport layers is shown in Figure 3. Figure 4 shows the energy band diagram of different hole transport layers. The numerical analysis using different kinds of hole transport layers, such as Spiro-OMeTAD, P3HT, CZTSe, PEDOT:PSS, CuI, and Cu_2O, has been conducted. Among all the HTL materials, Cu_2O has shown greater performance with increased device stability and overall efficiency.

4. Materials and Methods

4.1. SCAPS-1D Computer Simulation. The One-Dimensional Solar Cell Capacitance Simulator (SCAPS-1D) program was created by Prof. Marc Burgelman, a faculty of Electronics and Information Systems (ELIS) at the University of Ghent in Belgium [41]. This software is used to simulate semiconductor devices and involves solving through numerical methods [42, 43]. The equations are solved using Newton-Raphson substeps and Gummel iterative tackle. This approach enables the simulation of complex semiconductor systems and facilitates the analysis and optimization of semiconductor device performance. Overall, the development of

Table 1: The simulation material parameter of FTO/$PC_{60}BM$/$CsSn_{0.5}Ge_{0.5}I_3$/Cu_2O/Au model.

Parameters	FTO [37]	$PC_{60}BM$ (ETM) [38]	$CsSn_{0.5}Ge_{0.5}I_3$ (absorber) [39]	Cu_2O (HTM) [40]
Thickness (nm)	300	200	400	250
Eg (eV)	3.2	2	1.5	2.17
χe (eV)	4.4	3.9	3.9	3.2
ε	9	9	9	7.1
N_c (cm^{-3})	2.2×10^{18}	2.5×10^{19}	2.2×10^{18}	2×10^{17}
N_v (cm^{-3})	1.8×10^{19}	2.5×10^{19}	1.8×10^{19}	1.1×10^{19}
μ_e ($cm^2\ V^{-1}\ s^{-1}$)	90	0.2	974	200
μ_h ($cm^2\ V^{-1}\ s^{-1}$)	90	0.2	213	80
N_D (cm^{-3})	7×10^{20}	3×10^{17}	0	0
N_A (cm^{-3})	0	0	1×10^{14}	2×10^{18}
N_t (cm^{-3})	1×10^{15}	1×10^{15}	1×10^{14}	1×10^{15}

the SCAPS platform has been instrumental in advancing research in the field of semiconductor devices.

The elementary particle electron and vacancy equations for continuity are as follows [21]:

$$\begin{aligned} \frac{\partial J_{et}}{\partial x} - U_{et} + G_{et} &= 0, \\ -\frac{\partial J_{ht}}{\partial x} - U_{ht} + G_{ht} &= 0. \end{aligned} \tag{1}$$

The drift-diffusion equations for holes, as well as electrons, are outlined below:

$$\begin{aligned} J_{et} &= Qe(x)\mu_{et}E(x) + QD_{et}\frac{\det}{dx}, \\ J_{ht} &= Qh(x)\mu_{ht}E(x) + QD_{ht}\frac{dht}{dx}. \end{aligned} \tag{2}$$

The Poisson equation appears to resemble this:

$$\frac{d}{dx}\left(\frac{d\Psi}{dx}\right) = -\frac{Q}{\varepsilon}[Ht - Et + N_D^+(x) - N_A^-(x) + h_t(x) - e_t(x)]. \tag{3}$$

The symbols J_{et} and J_{ht} symbolize the current concentrations of both holes and electrons in a substance, respectively, and are connected to physical properties that govern how they behave. U_{et} and U_{ht} demonstrate the rates at which electrons and holes merge again, whereas G reflects the rate at which light forms a pair of electrons and holes.

The symbol Q represents electronic charge, and ψ represents the electrostatic potential. Furthermore, the letters Ht and Et are employed to designate the densities of liberated holes and electrons, correspondingly, in this article's nomenclature. Electron mobility and hole mobility are represented by the symbols e_t and h_t, respectively, whereas electrons and hole coefficients of diffusion are indicated by D_{et} and D_{ht}, respectively. N_D and N_A represent the charged donor and acceptor component densities, respectively. Finally, h_t and e_t reveal the concentrations of imprisoned holes and electrons, respectively.

4.2. Stability and Optoelectronic Property of $CsSn_{0.5}Ge_{0.5}I_3$. $CsSn_{0.5}Ge_{0.5}I_3$ is a lead-free perovskite material that has been shown to have good stability and optoelectronic properties. It is composed of cesium (Cs), tin (Sn), germanium (Ge), and iodine (I). $CsSn_{0.5}Ge_{0.5}I_3$ has been demonstrated to have a high optical absorption coefficient and to be stable in air and moisture [44]. This makes it a potentially useful material for solar cells, light-emitting diodes, and other optoelectronic gadgets. Here are some of the key stability and optoelectronic properties of $CsSn_{0.5}Ge_{0.5}I_3$.

4.2.1. Stability. $CsSn_{0.5}Ge_{0.5}I_3$ is stable in air and moisture, and it has a long shelf life. This makes it a more attractive material for use in solar cells and other devices than lead-based perovskites, which are known to be unstable in air and moisture [36].

4.2.2. Optical Absorption Coefficient. $CsSn_{0.5}Ge_{0.5}I_3$ has a high optical absorption coefficient, which means that it can absorb a lot of light. This makes it a good material for use in solar cells, where it can convert sunlight into electricity.

4.2.3. Bandgap. The bandgap of $CsSn_{0.5}Ge_{0.5}I_3$ is 1.5 eV, which is in the visible light range. This means that it can absorb visible light, which is the type of light that is most abundant in sunlight.

First, the following thermodynamic equilibrium needs to be reached to stabilize the $CsSn_{0.5}Ge_{0.5}I_3$ phase:

$$\Delta\delta_{Cs} + \Delta\delta_{\frac{1}{2}Sn} + \Delta\delta_{\frac{1}{2}Ge} + 3\Delta\delta_I \rightleftharpoons \Delta H(CsSn_{0.5}Ge_{0.5}I_3) = -14.12\ \text{eV}. \tag{4}$$

The symbol $\Delta H(CsSn_{0.5}Ge_{0.5}I_3)$ represents the energy change (enthalpy) during the formation of a compound called $CsSn_{0.5}Ge_{0.5}I_3$. This enthalpy is calculated concerning the initial elements: Cs (in a cubic structure with the space group *Fm3m*), Sn (in a cubic structure with the space group *Fd3m*), Ge (also in a cubic structure with the space group

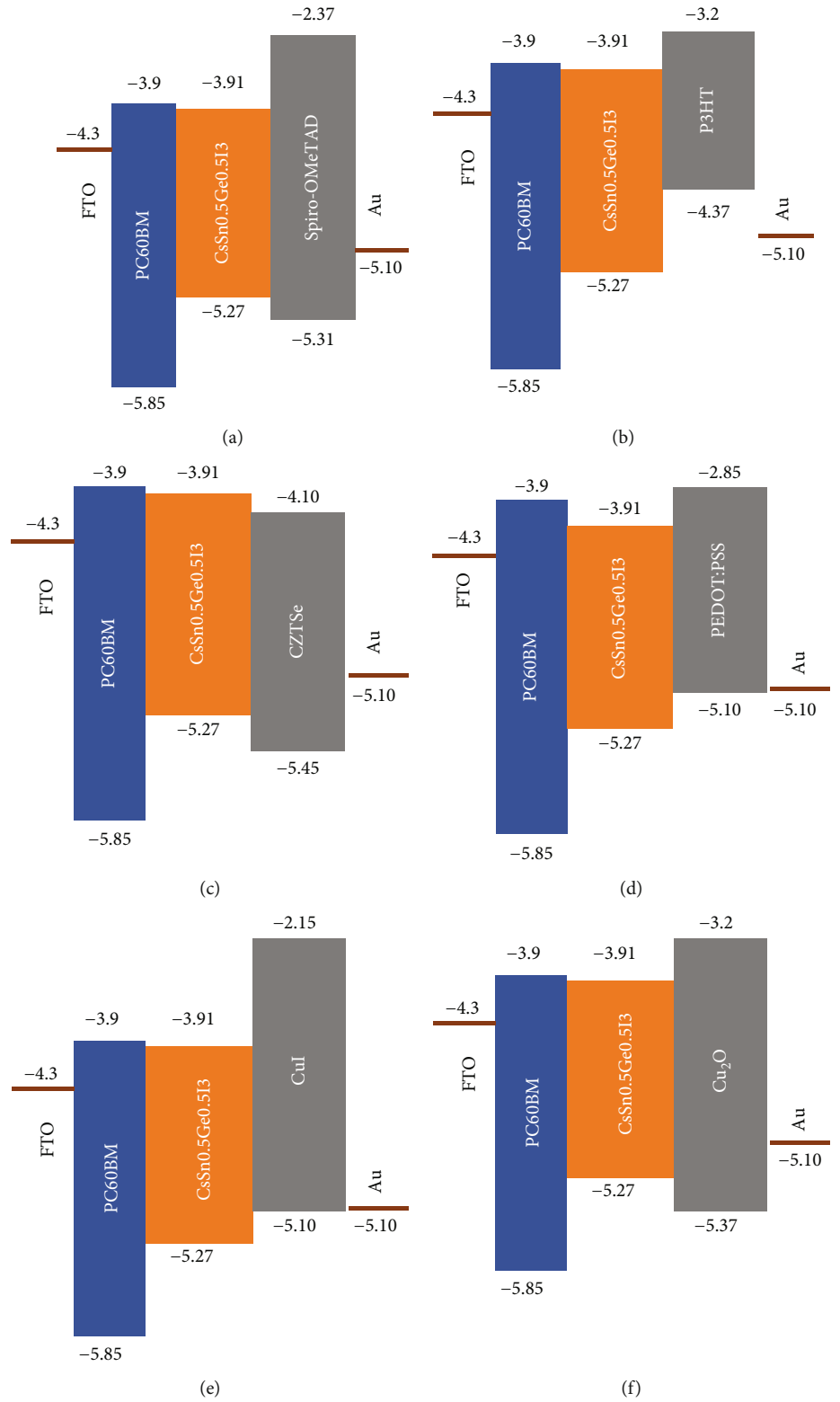

FIGURE 3: Energy band alignment diagram of different HTL for $CsSn_{0.5}Ge_{0.5}I_3$-based perovskite solar cell: (a) Spiro-OMeTAD, (b) P_3HT, (c) CZTSe, (d) PEDOT:PSS, (e) CuI, and (f) Cu_2O.

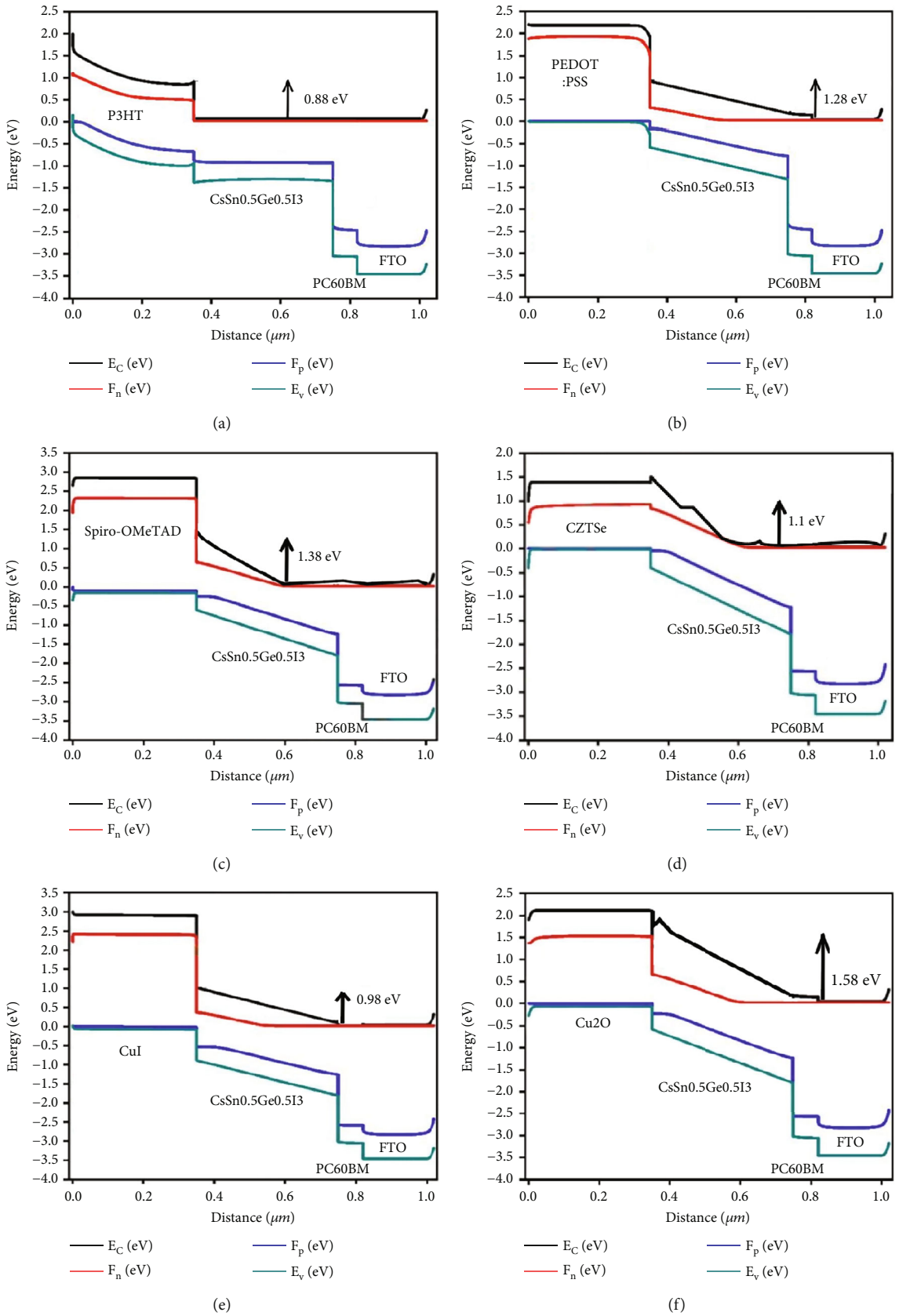

Figure 4: Energy band diagram of different HTL for $CsSn_{0.5}Ge_{0.5}I_3$-based perovskite solar cell: (a) P3HT, (b) PEDOT:PSS, (c) Spiro-OMeTAD, (d) CZTSe, (e) CuI, and (f) Cu_2O.

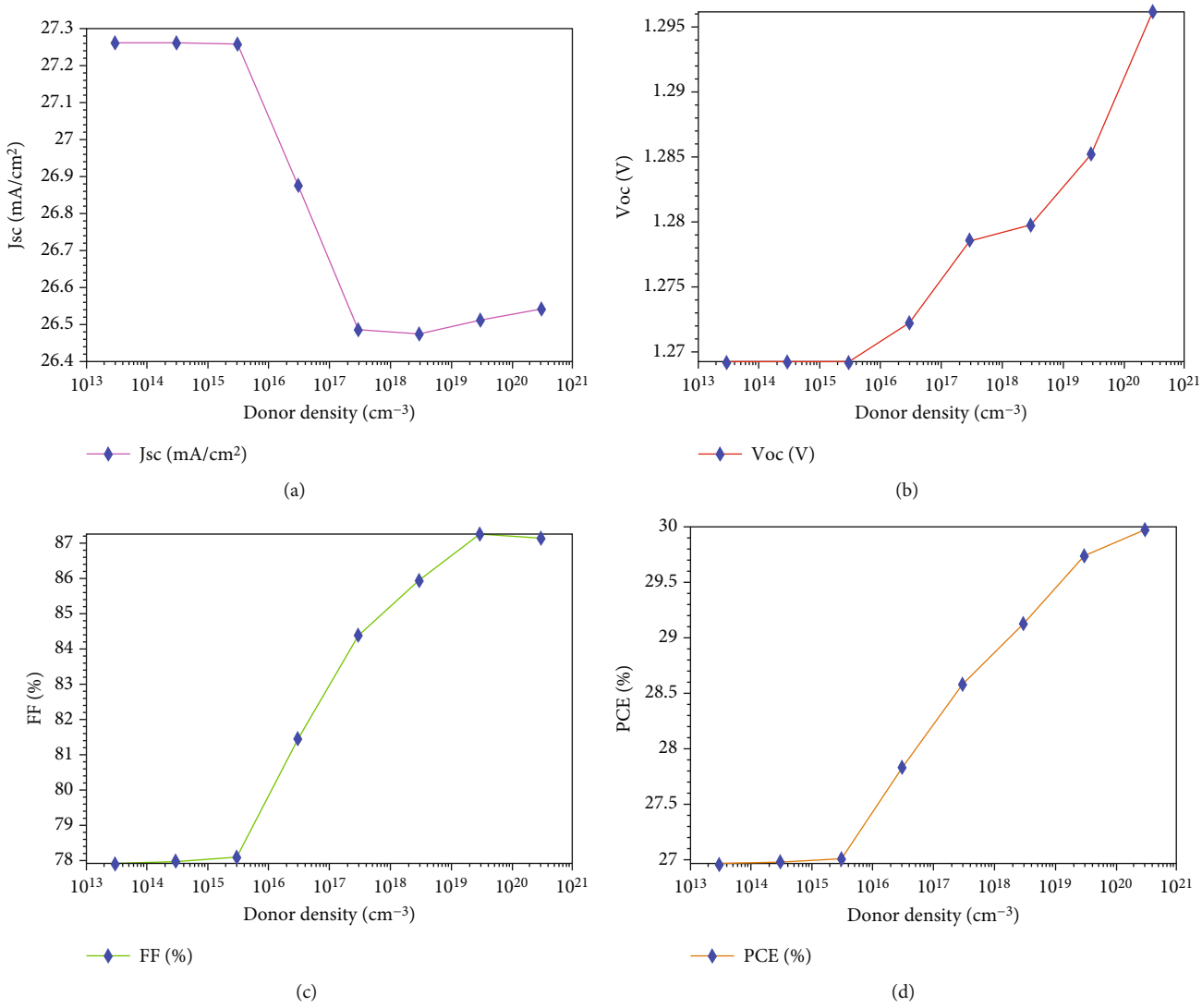

Figure 5: (a) J_{sc} (mA cm^{-2}), (b) V_{oc} (V), (c) FF (%), and (d) PCE (%) with varied $PC_{60}BM$ donor density (N_D) values.

Table 2: The device performance parameter value for $N_D = 10^{18}$ cm^{-3}.

Parameter structure	V_{oc} (V)	J_{sc} (mA cm^{-2})	FF (%)	PCE (%)
FTO/$PC_{60}BM$/$CsSn_{0.5}Ge_{0.5}I_3$/Cu_2O/Au	1.28	26.5	85.4	28.8

Fd3m), and I (in an orthorhombic structure with the space group *Immm*).

Second, it is necessary to exclude the fundamental phase:

$$\begin{aligned} \Delta\delta_{Cs} &< 0, \\ \Delta\delta_{Sn} &< 0, \\ \Delta\delta_{Ge} &< 0, \\ \Delta\delta_{I} &< 0. \end{aligned} \tag{5}$$

Furthermore, to avoid the formation of binary compounds and other undesired secondary phases, it is necessary to fulfill the following equations, which prevent the emergence of CsI (in a cubic structure with the space group *Fm-3m*), GeI_2 (in a rhombohedral structure with the space group *R3m*), SnI_2 (in a cubic structure with the space group *P-43m*), and SnI_4 (in a cubic structure with the space group *Pa-3*), as well as ternary compounds $CsGeI_3$ (in a rhombohedral structure with the space group *R3m*) and Cs_2SnI_6 (in a cubic structure with the space group *Fm-3m*) [13].

$$\begin{aligned} \Delta\delta_{Cs} + \Delta\delta_{I} &< \Delta H(\mathrm{CsI}) = -3.14\ \mathrm{eV}, \\ \Delta\delta_{Sn} + 2\Delta\delta_{I} &< \Delta H(\mathrm{SnI_2}) = -1.51\ \mathrm{eV}, \\ \Delta\delta_{Sn} + 4\Delta\delta_{I} &< \Delta H(\mathrm{SnI_4}) = -1.91\ \mathrm{eV}, \\ \Delta\delta_{Ge} + 2\Delta\delta_{I} &< \Delta H(\mathrm{GeI_2}) = -1.07\ \mathrm{eV}. \end{aligned} \tag{6}$$

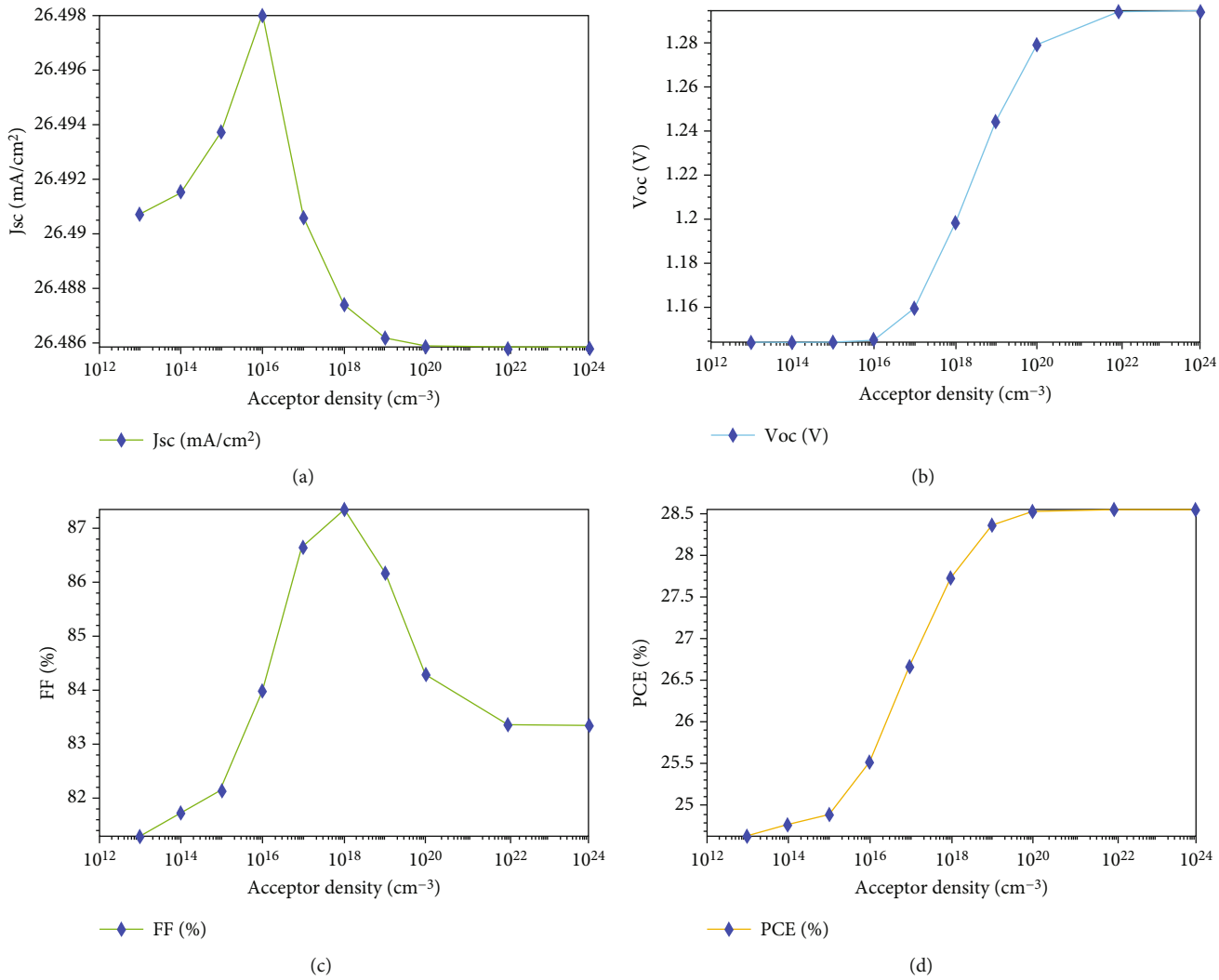

Figure 6: (a) J_{sc} (mA cm^{-2}), (b) V_{oc} (V), (c) FF (%), and (d) PCE (%) with varied Cu_2O acceptor density (N_A) values.

Table 3: The device performance parameter value for $N_A = 10^{19}$ cm^{-3}.

Parameter structure	V_{oc} (V)	J_{sc} (mA cm^{-2})	FF (%)	PCE (%)
FTO/$PC_{60}BM$/$CsSn_{0.5}Ge_{0.5}I_3$/Cu_2O/Au	1.25	26.48	86.5	28.4

To investigate the optical characteristics of $CsSn_{0.5}Ge_{0.5}I_3$, the amplified dielectric function is converted into the absorption coefficient to simulate the optical absorption spectrum, denoted as β_{abs}. This transformation is carried out using the following formula [13]:

$$\beta_{abs} = \sqrt{2_\theta}\left(\sqrt{\left(\varepsilon_1^2(\theta) + \varepsilon_2^2(\theta)\right)} - \varepsilon_1(\theta)\right)^{1/2}, \quad (7)$$

where $\varepsilon_1(\theta)$ and $\varepsilon_2(\theta)$ are the real and imaginary parts, respectively, of the complex dielectric function, which varies with frequency, denoted as $\varepsilon(\theta)$. Considering that the dielectric function is a tensor, $\varepsilon_1(\theta)$ and $\varepsilon_2(\theta)$ are averaged over three polarization vectors (along x, y, and z directions) [13]. The polyhedron in Figure 3 depicts the computed chemical potential window diagram and the region where $CsSn_{0.5}Ge_{0.5}I_3$ is stabilized against potential competing phases such as Ge, CsI, GeI_2, SnI_2, SnI_4, $CsGeI_3$, and Cs_2SnI_6.

5. Results and Discussion

5.1. The Influence of the Varying Ionized Donor Density (N_D) within the $PC_{60}BM$ Layer. It is critical to raise the conductivity of the $PC_{60}BM$ layer in a solar cell to boost its short-circuit current density (J_{sc}). However, the restricted electron mobility and fundamental electrical conductivity of $PC_{60}BM$ are limiting constraints. To counteract this, an optimum doping concentration may be used to improve the electrical characteristics of the $PC_{60}BM$ layer, increasing its conductivity and

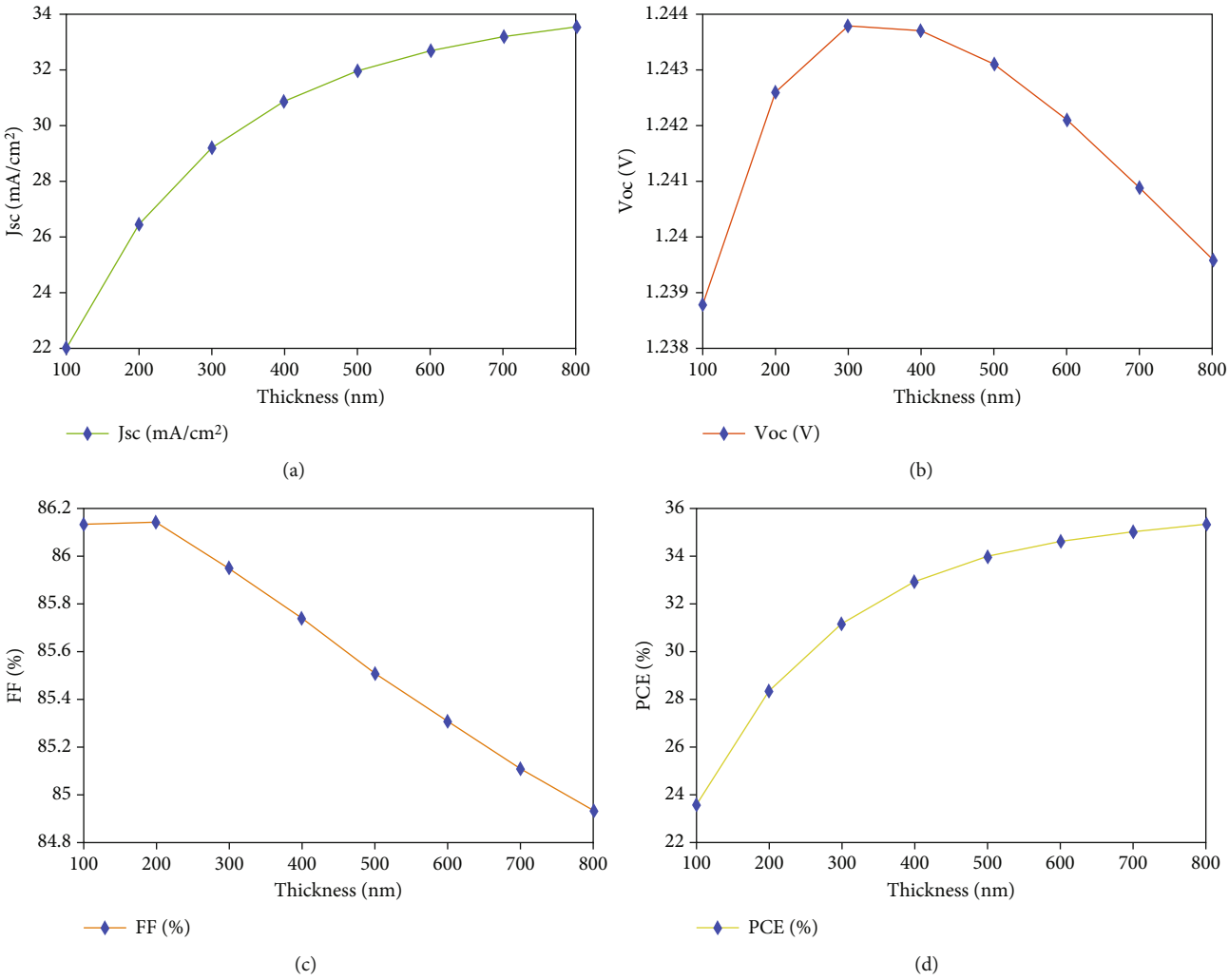

Figure 7: (a) J_{sc} (mA cm^{-2}), (b) V_{oc} (V), (c) FF (%), and (d) PCE (%) with varied thickness values of the absorber layer.

improving the J_{sc}. An appropriate level of $PC_{60}BM$ doping leads to the creation of a significant energy state at the interfaces of heterojunctions. This state serves to reduce nonradiative recombination, thus enhancing the overall efficiency of the system [45]. At relatively high and reasonable doping concentrations, a powerful electric field is generated. This field promotes electron collection while forcing minority carriers aside away from the ETL/perovskite contact. As a result, the rate of synthesis at the interface declines, leading to improved performance [45]. Figure 5 depicts the influence of various $PC_{60}BM$ doping doses on the effectiveness (PCE, FF, V_{oc}, and J_{sc}) of solar cells made from perovskite. It was discovered that increasing the electron transport layer's (ETL's) doping concentration (N_D) led to improvements in all of these parameters. This layer's donor concentration varied from 10^{13} to 10^{20} cm^{-3}. The short-circuit current density (J_{sc}) initially increased with higher doping concentrations, reaching a peak value of 27.28 mA/cm^2 at a doping concentration ranging from 10^{13} to 10^{14} cm^{-3}. At a doping concentration of approximately 10^{15} to 10^{17} cm^{-3}, the J_{sc} value shows a slight downshift value around 27.2 to 26.5 mA cm^{-2} and it remains almost constant at 26.55 mA cm^{-2} at 10^{18} to 10^{20} cm^{-3} as shown in Figure 5(a). Upon further investigation of additional parameters, such as the fill factor (FF), it was observed that as the doping concentration increased from 10^{15} to 10^{20} cm^{-3}, the FF exhibited an upward trend. The FF values were found to range from 78% to 87% within this doping concentration range. However, as the doping concentration was increased to 10^{20} cm^{-3}, the curve exhibited a slight decline, and the fill factor (FF) value stabilized at 87% for even higher doping concentrations. In terms of the power conversion efficiency (PCE), it has been observed that increasing the doping concentration from 10^{13} to 10^{20} cm^{-3} resulted in an upward shift of the PCE curve. Additionally, for the remaining portion of the increase, the PCE value remained stable at a consistent level of 28.5%.

Table 4: Device performance parameter value, for 490 nm of the absorber layer width.

Thickness (nm)	V_{oc} (V)	J_{sc} (mA cm^{-2})	FF (%)	PCE (%)
490	1.242	31.7	85.5	33.8

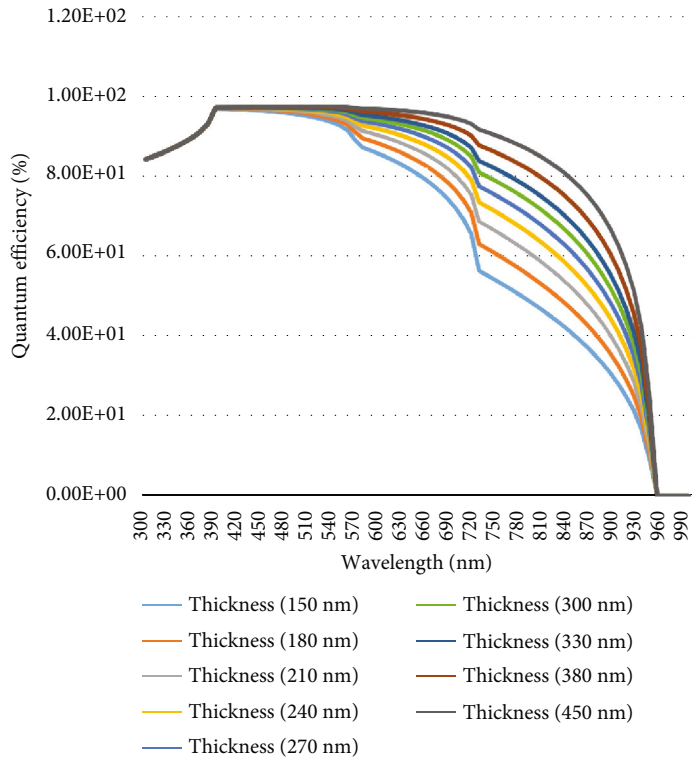

Figure 8: Quantum efficiency with varying thickness value.

Doping boosts the conductive properties of the $PC_{60}BM$ layer, which is advantageous for cell functionality. If the doping concentration is overly high, the adverse consequences of contaminant diffusion might balance the benefits of doping, resulting in a decrease in the mobility of carriers. High doping levels may also result in the generation of deep coulomb traps, which may limit the mobility of charge carriers even further and have an adverse effect on short-circuit current density as well [46, 47]. Finally, a doping dose of $10^{18}\,cm^{-3}$ is selected, and the outcomes of enhanced parameters are presented in Table 2.

5.2. Effect of Cu_2O Layer Acceptor Density (N_A). The acceptor concentration inside the Cu_2O layer, designated as N_A, can have a considerable influence on perovskite solar cell effectiveness. According to research, increasing the acceptor density can enhance the solar cell's fill factor (FF) and power conversion efficiency (PCE). This is because a greater acceptor density increases the number of holes that can be retrieved from the perovskite layer, leading to a higher current density and greater efficiency [48]. However, there is a limit to the benefits of increasing the acceptor density, as excessively high acceptor densities can result in a decrease in the PCE. This is due to the formation of a barrier that inhibits the flow of electrons from the perovskite layer to the electrode [49]. As depicted in Figure 6, it is evident that as the density of the absorber material is augmented from 10^{13} to $10^{16}\,cm^{-3}$, the open-circuit voltage (V_{oc}) persistently remains constant at 1.14 volts.

However, upon a further increase in density from 10^{16} to $10^{22}\,cm^{-3}$, the V_{oc} value exhibits a conspicuous upward shift, culminating in a remarkable rise to 1.30 volts, and remains in a steady state. For values ranging from 10^{13} to $10^{18}\,cm^{-3}$, both the fill factor (FF) and power conversion efficiency (PCE) demonstrate an upward shift. However, upon further increasing the doping concentration, the FF displays a downward trend, decreasing from 87.2% to 83%. In contrast, the PCE attains a steady-state value. These findings strongly show that increased doping concentrations have an adverse effect on the FF of solar cells. On the other hand, J_{sc} demonstrates a large upward movement as a result of a shift in acceptor density from 10^{13} to 10^{16}, leading to an increase in the photocurrent from 26.491 to 26.496 mA cm^{-2}. Subsequently, a downward shift in the photocurrent is observed for the doping concentration of 10^{16} to $10^{20}\,cm^{-3}$. Table 3 shows the consequent improvement attributes after which it remains in a stable state.

5.3. The Effect of Changing the Absorbing Layer's Properties. Efficient solar cell design requires meticulous selection of the absorber's parameters, with the depth of the active layer being a crucial factor in maximizing performance. Proper consideration must be given to this parameter since extremely thin active layers will lead to minimal light absorption.

Conversely, overly thick active layers will cause charge carrier recombination, particularly as the carriers travel a great distance before exiting the absorber layer [50]. Hence, to achieve optimal solar cell efficiency, careful attention must be paid to selecting the appropriate thickness for the active layer [51]. From the graphical data in Figure 7, the relation of V_{oc}, J_{sc}, FF, and PCE with the thickness value of the absorber layer can be seen. The thickness value has varied

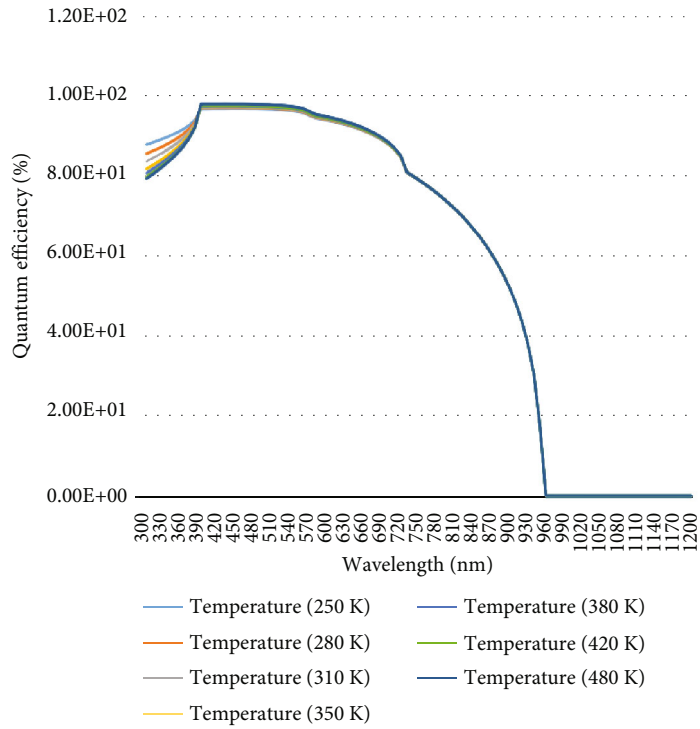

Figure 9: Quantum efficiency on various temperature.

within the range of 100 nm to 800 nm. The curve for J_{sc} and PCE values indicates an upward movement with increasing absorber layer depth until it accomplishes a steady-state value of 32.8 mA cm^{-2} for J_{sc} and 34.7% for PCE. On the other hand, the V_{oc} value spikes at 300 nm of thickness, and if the V_{oc} value is 1.24 V, it implies a decrease in voltage to boost the absorber layer depth. An interesting phenomenon has been seen in FF graphical curve. By varying the thickness towards increment, the value of FF shows a downshift and reaches 86.2% to 85% for the thickness of 100 nm to 800 nm. As a result, it is seen that varying thickness affects the PCE and J_{sc} most and thickness variation causes a massive impact on these two parameters. On the other hand, other parameters (FF and V_{oc}) indicate a minor variance owing to the change in the thickness of the absorber layer. So taking this effect in mind, we have set the thickness value at 490 nm as shown in Table 4.

5.4. The Effect of Varying Thickness Value on Quantum Efficiency. In this study, the investigation of the quantum efficiency (QE) characteristics of $CsSn_{0.5}Ge_{0.5}I_3$ perovskite absorber layer to varying thickness has been conducted.

A comprehensive analysis of QE (%) across a range of wavelengths, from 300 nm to 1000 nm, was conducted and is shown in Figure 8. These findings reveal a notable trend wherein the QE remains consistently high, exceeding 80%, within the wavelength range of 300 nm to 860 nm.

This indicates efficient photon absorption and charge carrier generation within this broad region of the solar spectrum. Beyond this range, a gradual decline in QE is observed, suggesting a shift in the absorption properties of the perovskite material. These results underscore the potential of $CsSn_{0.5}Ge_{0.5}I_3$ perovskite as a promising absorber material for solar cell applications, particularly in harnessing a substantial portion of solar radiation for energy conversion.

Table 5: The efficacy parameter's value swings as the absorber defect density varies.

Defect density (cm^{-3})	V_{oc} (V)	J_{sc} (mA cm^{-2})	FF (%)	PCE (%)
10^{13}	1.2738	31.865	85.10	34.54
10^{14}	1.1907	31.865	82.94	31.47
10^{15}	1.0758	31.865	81.91	28.08

Table 6: Effect of different electron transport materials on the performance parameter.

ETL materials	V_{oc} (V)	J_{sc} (mA cm^{-2})	FF (%)	PCE (%)
TiO_2	1.29	25.46	85.57	28.11
ZnO	1.27	24.46	84.47	26.22
IGZO	1.29	25.36	86.33	28.29
$Cd_{0.5}Zn_{0.5}S$	1.2929	25.5022	84.85	27.98
C_{60}	1.25241	18.688	85.08	19.91
CDs	1.0837	25.61	81.38	22.59
$PC_{60}BM$	1.31	26.57	86.27	29.95

5.5. The Effect of Varying Temperature on Quantum Efficiency. This study explored the impact of temperature on the light absorption properties of $CsSn_{0.5}Ge_{0.5}I_3$ perovskite material. This investigation shows the relationship

Table 7: Electron transport material (ETM) characteristics for different substances.

Parameters	ZnO [54, 55]	TiO_2 [56]	CdS [57]	C_{60} [58, 59]	$Cd_{0.5}Zn_{0.5}S$ [60]	IGZO [61]
Eg (eV)	3.3	3.2	2.4	1.7	2.8	3.05
χe (eV)	4.1	3.9	4.2	3.9	3.8	4.16
E	9	9	10	4.2	10	10
N_C (cm^{-3})	4×10^{18}	1×10^{21}	2.2×10^{18}	8×10^{19}	1×10^{18}	5×10^{18}
N_V (cm^{-3})	1×10^{19}	2×10^{20}	1.8×10^{19}	8×10^{19}	1×10^{18}	5×10^{18}
μ_e ($cm^2\ V^{-1}\ s^{-1}$)	100	20	20	0.08	100	15
μ_h ($cm^2\ V^{-1}\ s^{-1}$)	25	10	10	0.0035	25	0.1
N_D (cm^{-3})	1×10^{18}	1×10^{17}	1×10^{17}	2.6×10^{18}	1×10^{17}	1×10^{18}
N_A (cm^{-3})	0	0	0	0	0	0
N_t (cm^{-3})	1×10^{15}	1×10^{15}	1×10^{17}	1×10^{14}	1×10^{15}	1×10^{15}

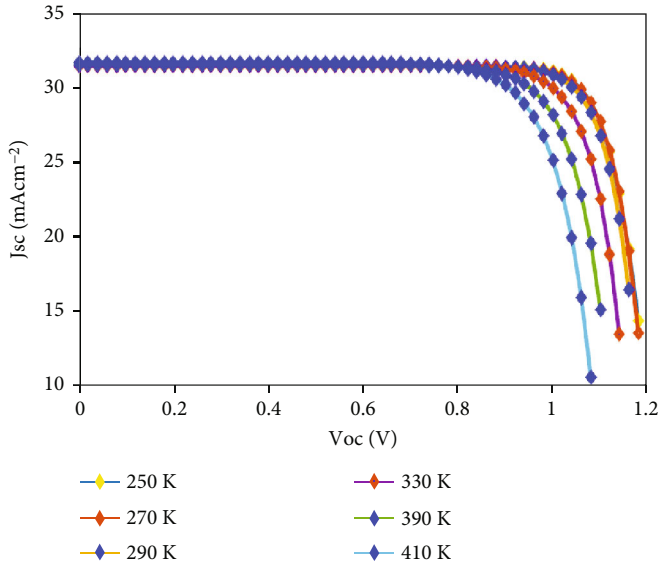

Figure 10: Effect of operating temperature on J-V characteristics.

between wavelength and quantum efficiency (QE) across a temperature range of 250 K to 480 K.

The results revealed remarkable stability in the material's light absorption across a significant portion of the visible spectrum. Figure 9 shows that within the 300 nm to 740 nm wavelength range, the QE remained consistently above 80% for all studied temperatures. This indicates efficient light capture within the visible light spectrum, a crucial characteristic for effective solar cell operation. A slight decrease in QE has been noticed from 300 nm to 390 nm wavelength along with the increment of temperature value of the incident light. This minor change in the QE value can be seen in the figure. The QE remained high across a broad range, and a slight decrease was observed beyond 740 nm wavelength after increasing the temperature above 450 K.

Overall, this study highlights the potential of $CsSn_{0.5}Ge_{0.5}I_3$ as a temperature-stable light absorber for solar cell applications. The observed high QE across a wide range of visible wavelengths and its resilience to temperature variations are promising findings.

Table 8: Operating temperature effect on performance.

Temperature (K)	V_{oc} (V)	J_{sc} (mA cm^{-2})	FF (%)	PCE (%)
250	1.2274	31.3919	82.24	31.69
270	1.2141	31.405	82.96	31.63
290	1.2004	31.4143	82.8	31.22
330	1.1716	31.4306	81.32	29.95
370	1.1409	31.48	79.48	28.55
410	1.1074	31.6616	77.71	27.24

5.6. The Effect of Defect Density. The measure of defect density, denoted as N_t, is a pivotal factor in governing the electrical properties of materials and thus has the potential to make a substantial contribution to enhancing the efficiency

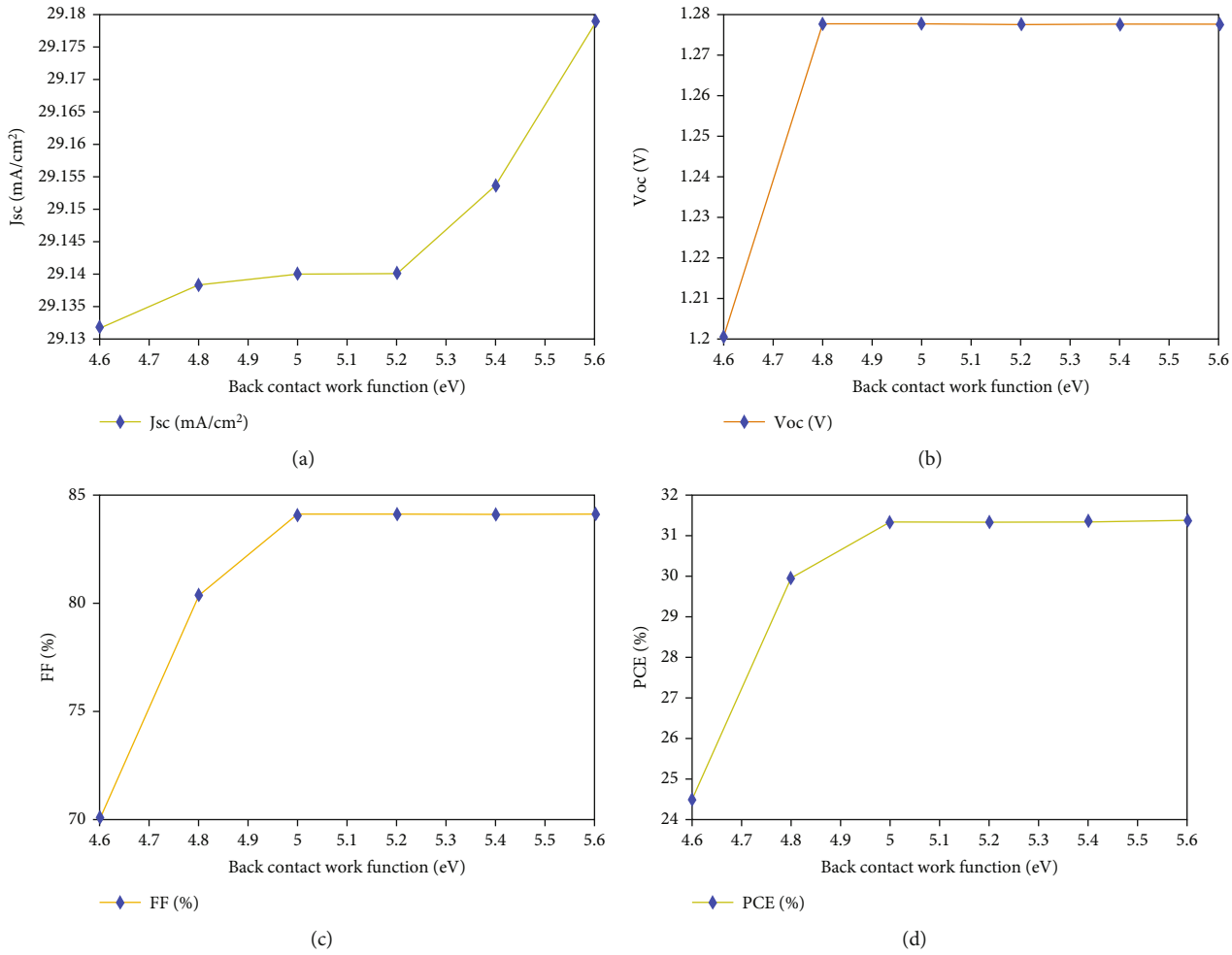

Figure 11: (a) J_{sc} (mA cm^{-2}), (b) V_{oc} (V), (c) FF (%), and (d) PCE (%) with the varied work function value of the back contact.

of solar cells [52]. To achieve top-notch performance, it becomes indispensable to enhance the quality of the absorbing layer. It has been observed that the performance of a device escalates proportionately with a decrease in the defect density, as evidenced by Table 5.

However, in practice, it poses a formidable challenge to fabricate materials with defect densities as low as 10^{13} cm^{-3} [53]. On the contrary, a value of $N_t = 1015$ cm^{-3} allows for the attainment of optimal efficiency in solar cells, although there is no noticeable variation in J_{sc} and V_{oc}, despite a decrease in defect density from 10^{15} to 10^{13} cm^{-3} in the resultant. Table 5 displays the requirements for improvement.

5.7. Effect of Different Electron Transport Material. To improve the performance of the proposed $CsSn_{0.5}Ge_{0.5}I_3$-based perovskite solar cell, several electron transport materials (ETMs) such as ZnO, TiO_2, CdS, C_{60}, $Cd_{0.5}Zn_{0.5}S$, and IGZO were used. It has been found that among all the ETL materials, $PC_{60}BM$ has shown the greater efficiency, which is shown in Figure 1. Table 6 summarizes the important performance metrics for each ETM. The characteristic parameter for different ETL materials is shown in Table 7. The performance difference is due to a conduction band offset between the ETL/perovskite absorber interface and greater carrier mobility.

5.8. The Influence of Temperature Settings on Performance Parameters. A solar cell's efficiency is profoundly affected by its functioning temperature. Despite a solar cell's usual operating temperature of 300 K, its temperature during operation will be significantly greater. Figure 10 illustrates that the temperature variation can have a substantial effect on the PV cell's J-V curves. Open-circuit voltage (V_{oc}) drops significantly with a temperature rise, while J_{sc} only increases marginally.

This is due to a larger reverse saturation current, which causes a decrease in V_{oc}. Furthermore, when temperature rises, the bandgap of the semiconductor decreases, resulting in a modest increase in J_{sc}. According to the J-V graph, rising temperature diminishes the output of PV cells due to the decrease in V_{oc}. Besides this, increased temperature alters the characteristics of PV cells, such as the mobility and concentration of charge carriers, resistance, and bandgap of materials.

Table 8 unequivocally demonstrates that as the temperature rises from 250 K, there is a substantial decline in voltage, while the current density (J_{sc}) experiences a consistent increase. Conversely, both power conversion efficiency

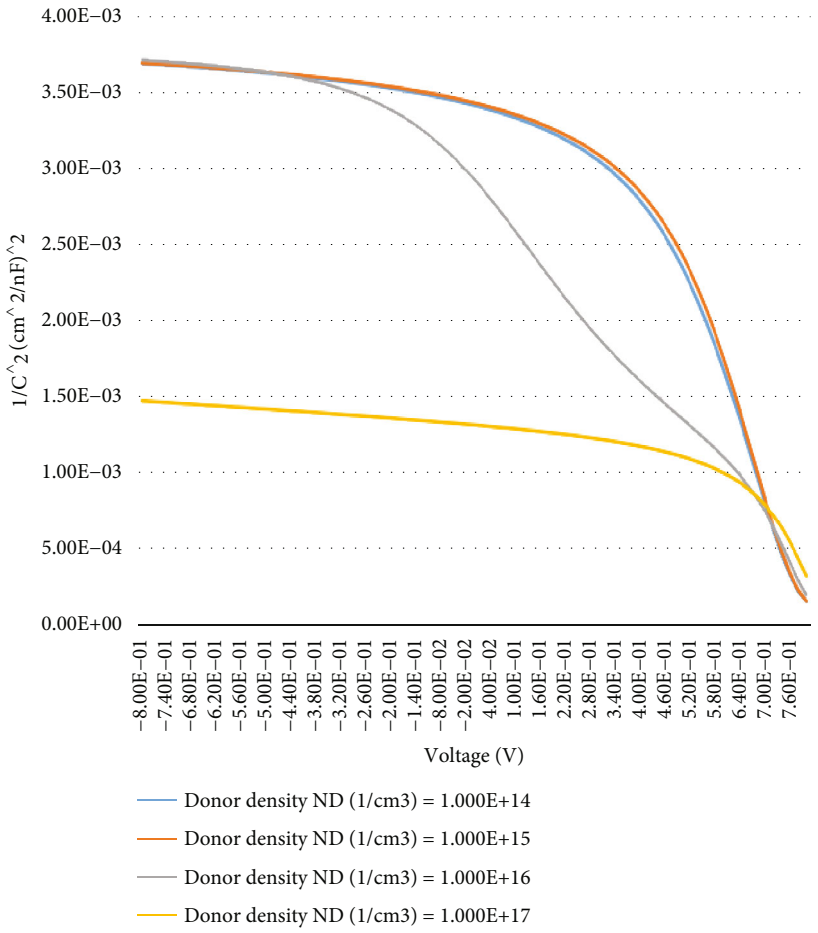

Figure 12: The Mott-Schottky capacitance characteristic plot.

(PCE) and fill factor (FF) exhibit a significant reduction in value with the escalating temperature.

5.9. The Effect of Back Contact Work Function. To achieve excellent efficiency in solar cells made from perovskite, one must choose a proper rear interface substance with an outstanding function [62]. Recent research has demonstrated that by altering the rear contact work function utilizing interface engineering and leveraging low-work function materials, perovskite solar cells may be far more effective [63]. A more extensive function rear contact, on the contrary, could end up in a deeper energy obstacle, leading to greater crossover inefficiencies and influencing the cell's overall effectiveness. Therefore, careful consideration must be given to selecting the appropriate back contact material and modifying its work function to achieve optimal performance in perovskite solar cells.

This analysis finds that for work function values more than 5 eV, the values of the V_{oc}, FF, and PCE curves exhibit an upward shift and stay in a steady state. The J_{sc} value, on the other hand, gradually increases with decreasing work function values (<5 eV). However, once the work function value exceeds 5 eV, the J_{sc} value abruptly changes, resulting in high current density values as shown in Figure 11.

Table 9: Final optimized performance parameter values for FTO/$PC_{60}BM$/$CsSn_{0.5}Ge_{0.5}I_3$/Cu_2O/Au structure.

V_{oc} (V)	1.12
J_{sc} (mA cm^{-2})	31.56
FF (%)	81.47
PCE (%)	27.72

5.10. Mott-Schottky Capacitance Characteristics. The Mott-Schottky capacitance characteristic has been analysed numerically which has been shown in Figure 12. The variation of donor density of the electron transport material has been carried out from a range of 10^{14} to 10^{17} cm^{-3}. It has been found that the donor density value of the $PC_{60}BM$ electron transport material has the most significant influence on this particular analysis. The visual result of this analysis has been shown in Figure 12.

5.11. Final Optimized Performance Parameter. This research has achieved exceptional performance parameters for the FTO/$PC_{60}BM$/$CsSn_{0.5}Ge_{0.5}I_3$/Cu_2O/Au solar cell configuration. The open-circuit voltage (V_{oc}) was measured at 1.12 V, indicating a high voltage potential. The current density recorded was 31.56 mA cm^{-2}, representing a significant

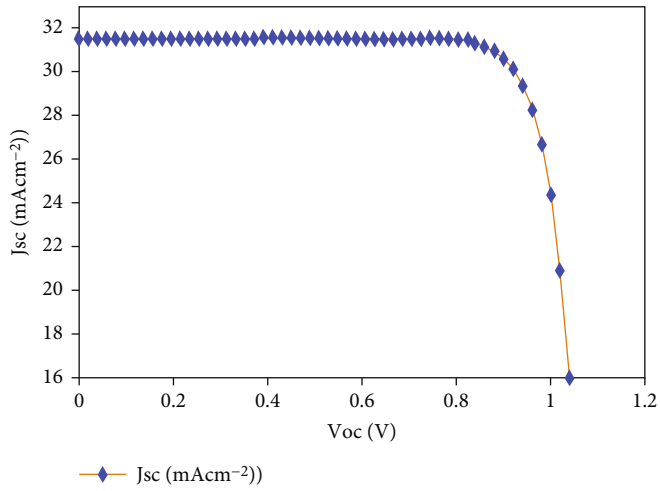

Figure 13: Final optimized result.

flow of current. The fill factor (FF) reached an impressive value of 81.47%, indicating efficient charge transfer and minimal losses within the device which is shown in Table 9. Finally, the photovoltaic conversion efficiency (PCE) achieved an outstanding value of 27.72%, signifying the effectiveness of the solar cell in converting sunlight into electricity.

These remarkable results are visually presented in Figure 13, which displays the graphical representation of the obtained data. The figure further illustrates the excellent performance and demonstrates the correlation between the different parameters, highlighting the efficiency and viability of the proposed solar cell configuration.

6. Conclusion

This study has been carried out to analyze numerous variables of the perovskite photovoltaic cell structure FTO/$PC_{60}BM$/$CsSn_{0.5}Ge_{0.5}I_3$/Cu_2O/Au. This research has been conducted to analyze the effect of Cu_2O as a hole transport layer with $CsSn_{0.5}Ge_{0.5}I_3$ perovskite material. The SCAPS-1D tool was employed in the present investigation to carry out computational simulations to find out the influence in boosting the photovoltaic energy production and characteristics of the photovoltaic cell. This research numerically analyze the effect of changing absorbing material layer thickness, defect density, donor and acceptor densities of the charge transport layers, anode work function, and operating temperature on the performance parameter. It has been found that the ETL and HTL pumping concentrations have significant impacts on the effectiveness of the perovskite solar cell, with a higher doping concentration leading to a boost in V_{oc} and PCE due to enhanced conductivity and quasi-Fermi dissociation levels. Here, Cu_2O is a great candidate as a hole transport layer in this model. Similarly, ensuring a sufficient number of defects in the absorber layer and choosing appropriate work functions for the anode significantly improves the performance of the perovskite solar cell. The results illustrate the detrimental impact of temperature on solar cell effectiveness, while a boost in temperature from 250 K to 410 K triggers an overall reduction in efficiency. After optimizing all the aforementioned factors, the perovskite solar cell attains a high level of performance, with a PCE of 27.72%, FF of 81.47%, 31.56 mA cm^{-2}, and V_{oc} of 1.12 V. Overall, the data presented in this study showcases the remarkable performance of the solar cell, characterized by high V_{oc}, current density, fill factor, and photovoltaic conversion efficiency. These outcomes validate the effectiveness and potential of the chosen configuration.

Data Availability

The experimental data used to support the findings of this study are included within the article.

Conflicts of Interest

The authors declare that there are no conflicts of interest associated with publishing this work.

Acknowledgments

The authors would like to extend their acknowledgment to Gent University, Belgium, for developing and providing the SCAPS-1D simulator used in this work.

References

[1] N. Thakur, K. A. Aly, M. Mohery, M. M. Ebrahium, P. Kumar, and P. Sharma, "Recent advances in BaZrS3 perovskites: synthesis, properties, and future trends," *Journal of Alloys and Compounds*, vol. 957, article 170457, 2023.

[2] N. Thakur, P. Kumar, and P. Sharma, "Simulation study of chalcogenide perovskite (BaZrSe3) solar cell by SCAPS-1D," *Materials Today: Proceedings*, 2023, https://www.sciencedirect.com/science/article/pii/S2214785323000226.

[3] N. Thakur, P. Kumar, R. Neffati, and P. Sharma, "Design and simulation of chalcogenide perovskite $BaZr(S,Se)_3$ compositions for photovoltaic applications," *Physica Scripta*, vol. 98, no. 6, article 065921, 2023.

[4] F. H. Isikgor, S. Zhumagali, and L. V. T. Merino, "Molecular engineering of contact interfaces for high-performance

perovskite solar cells," *Nature Reviews Materials*, vol. 8, no. 2, pp. 89–108, 2023.

[5] M. K. A. Mohammed, A. K. Al-Mousoi, and S. Singh, "Improving the performance of perovskite solar cells with carbon nanotubes as a hole transport layer," *Optical Materials*, vol. 138, no. 925-3467, article 113702, 2023.

[6] Y. Gao, F. Ren, D. Sun et al., "Elimination of unstable residual lead iodide near the buried interface for the stability improvement of perovskite solar cells," *Energy & Environmental Science*, vol. 16, no. 5, pp. 2295–2303, 2023.

[7] S. Motavassel, M. Seifouri, and S. Olyaee, "Efficiency improvement of perovskite solar cell by modifying structural parameters and using Ag nanoparticles," *Applied Physics A*, vol. 127, no. 2, 2021.

[8] S. Bhattarai, R. Pandey, J. Madan et al., "Numerical investigation of toxic free perovskite solar cells for achieving high efficiency," *Materials Today Communications*, vol. 35, article 105893, 2023.

[9] P. C. Bharti, P. K. Jha, P. A. Jha, and P. Singh, "Observation of isomorphic phase transition in non-perovskite green CsSnI 3," *Materialia*, vol. 27, article 101646, 2023.

[10] J. Pascual, G. Nasti, M. H. Aldamasy et al., "Origin of Sn(II) oxidation in tin halide perovskites," *Materials Advances*, vol. 1, no. 5, pp. 1066–1070, 2020.

[11] L. Lanzetta, T. Webb, N. Zibouche et al., "Degradation mechanism of hybrid tin-based perovskite solar cells and the critical role of tin (IV) iodide," *Nature Communications*, vol. 12, no. 1, p. 2853, 2021.

[12] V. D. Patel and D. Gupta, "Solution-processed metal-oxide based hole transport layers for organic and perovskite solar cell: a review," *Materials Today Communications*, vol. 31, no. 103664, pp. 2352–4928, 2022.

[13] Z. Wu, X. Xu, Y. Gao et al., "Remarkable stability and optoelectronic properties of an all-inorganic $CsSn_{0.5}Ge_{0.5}I_3$ Perovskite solar cell," *The Journal of Physical Chemistry Letters*, vol. 14, no. 1, pp. 302–309, 2023.

[14] P. Roy, A. Khare, S. Tiwari, and A. Mahapatra, "Revealing the role of band offsets on the charge carrier dynamics of $CsSn_{0.5}Ge_{0.5}I_3$-based perovskite solar cell: a theoretical study," *Energy Technology*, vol. 11, no. 8, article 2300253, 2023.

[15] T. Shen, "Study on perovskite photovoltaic materials and photovoltaic performance of perovskite solar cells," *Highlights in Science, Engineering and Technology*, vol. 26, pp. 29–33, 2022.

[16] V. Saetang, H. Qi, T. Smerchit, and N. Rujisamphan, "Laser scribing of fluorine-doped tin oxide coated on glass substrate in air and water," *Optics & Laser Technology*, vol. 153, article 108280, 2022.

[17] H. Heffner, M. Soldera, F. Ränke, and A. F. Lasagni, "Surface modification of fluorine-doped tin oxide thin films using femtosecond direct laser interference patterning: a study of the optoelectronic performance," *Advanced Engineering Materials*, vol. 25, no. 10, article 2201810, 2023.

[18] F. Wu, S. Lu, C. Hu et al., "A smart way to prepare solution-processed and annealing-free PCBM electron transporting layer for perovskite solar cells," *Advanced Sustainable Systems*, vol. 6, no. 9, article 2200212, 2022.

[19] S. Biswas, Y. Lee, H. Choi, H. W. Lee, and H. Kim, "Progress in organic photovoltaics for indoor application," *RSC Advances*, vol. 13, no. 45, pp. 32000–32022, 2023.

[20] A. Jain, R. Kothari, and R. Kumar Rajamony, "Advances in organic solar cells: materials, progress, challenges and amelioration for sustainable future," *Sustainable Energy Technologies and Assessments*, vol. 63, article 103632, 2024.

[21] S. Bouazizi, W. Tlili, A. Bouich, B. M. Soucase, and A. Omri, "Design and efficiency enhancement of FTO/PC_{60}BM/$CsSn_{0.5}Ge_{0.5}I_3$/Spiro-OMeTAD/Au perovskite solar cell utilizing SCAPS-1D simulator," *Materials Research Express*, vol. 9, no. 9, 2022.

[22] L. M. Merlin Livingston, R. T. Prabu, R. Radhika, and A. Kumar, "Simulation of native oxide-passivated $CsSn_{0.5}Ge_{0.5}I_3$ highly stable lead-free inorganic perovskite solar cell," *Physica Status Solidi (A)*, vol. 220, no. 14, 2023.

[23] S. Aseena, N. Abraham, G. Sahaya Dennish Babu, S. Kathiresan, and V. Suresh Babu, "Solution-synthesized Cu_2O as a hole transport layer for a ZnO-based planar heterojunction perovskite solar cell fabricated at room temperature," *Journal of Electronic Materials*, vol. 51, no. 4, pp. 1692–1699, 2022.

[24] S. Venkatesan, H. Teng, and Y.-L. Lee, "High performance photoelectrodes prepared using Au@ P3HT composite nanoparticles for dye-sensitized solar cells," *Journal of Alloys and Compounds*, vol. 926, article 166822, 2022.

[25] M. Wang, Y. Li, and X. Zhao, "Rational design of additive with suitable functional groups toward high-quality $FA_{0.75}MA_{0.25}SnI_3$ films and solar cells," *Solar RRL*, vol. 6, no. 1, article 2100800, 2023.

[26] S. Bouazizi and W. Tlili, "Methylammonium lead triiodide perovskite-based solar cells efficiency: insight from experimental and simulation," *Nano Energy*, vol. 122, pp. 1093–3263, 2023.

[27] M. Chen, M. G. Ju, H. F. Garces et al., "Highly stable and efficient all-inorganic lead-free perovskite solar cells with native-oxide passivation," *Nature Communications*, vol. 10, no. 1, p. 16, 2019.

[28] T. Ahmed and S. Subrina, "Novel hybrid monolayers $Si_xGe_ySn_{1-x-y}$: first principles study of structural, electronic, optical, and electron transport properties with NH_3 sensing application," *Physical Chemistry Chemical Physics*, vol. 24, no. 16, pp. 9475–9491, 2022.

[29] J. L. Prasanna, E. Goel, A. Kumar, and A. Kumar, "Computational study of perovskite/perovskite lead-free tandem solar cell devices," in *2022 IEEE International Symposium on Smart Electronic Systems (iSES)*, pp. 257–262, Warangal, India, 2022.

[30] C.-H. Chen, S.-N. Cheng, and L. Cheng, "Toxicity, leakage, and recycling of lead in perovskite photovoltaics," *Advanced Energy Materials*, vol. 13, no. 14, pp. 1614–6832, 2023.

[31] G.-Y. Kim, K. Kim, and H. S. Jung, "Sustainable and environmentally viable perovskite solar cells," *EcoMat*, vol. 5, no. 4, 2023.

[32] A. Bouich, J. Marí-Guaita, B. M. Soucase, and P. Palacios, "Bright future by enhancing the stability of methylammonium lead triiodide perovskites thin films through Rb, Cs and Li as dopants," *Materials Research Bulletin*, vol. 163, article 112213, 2023.

[33] J. Verheyen, V. Delnat, and C. Theys, "Daily temperature fluctuations can magnify the toxicity of pesticides," *Current Opinion in Insect Science*, vol. 51, article 100919, 2022.

[34] T. de Vrijer and K. Roodenburg, "PECVD processing of low bandgap-energy amorphous hydrogenated germanium-tin (a-GeSn:H) films for opto-electronic applications," *Applied Materials Today*, vol. 27, no. 1, pp. 2352–9407, 2022.

[35] M. Ikram, R. Malik, and M. Imran, "Recent advancements and future insight of lead-free non-toxic perovskite solar cells for sustainable and clean energy production: a review," *Sustainable*

Energy Technologies and Assessments, vol. 53, article 102433, 2022.

[36] A. Bouich and K. Koné, "Surface engineering of zinc oxide thin as an electron transport layer for perovskite solar cells," *Optical and Quantum Electronics*, vol. 55, no. 7, p. 574, 2023.

[37] D. Masekela, N. C. Hintsho-Mbita, B. Ntsendwana, and N. Mabuba, "Thin films (FTO/$BaTiO_3$/AgNPs) for enhanced piezo-photocatalytic degradation of methylene blue and ciprofloxacin in wastewater," *ACS Omega*, vol. 7, no. 28, pp. 24329–24343, 2022.

[38] N. Lakhdar and H. Abdelkader, "Electron transport material effect on performance of perovskite solar cells based on $CH_3NH_3GeI_3$," *Optical Materials*, vol. 99, article 109517, 2020.

[39] R. Raghvendra, R. Kumar, and S. K. Pandey, "Performance evaluation and material parameter perspective of eco-friendly highly efficient CsSnGeI3 perovskite solar cell," *Superlattices Microstruct*, vol. 135, article 106273, 2019.

[40] T.-H. Chuang, Y.-H. Chen, and S. Sakalley, "Highly stable and enhanced performance of p-i-n perovskite solar cells via cuprous oxide hole-transport layers," *Nanomaterials*, vol. 13, pp. 2079–4991, 2023.

[41] M. Burgelman, P. Nollet, and S. Degrave, "Modelling polycrystalline semiconductor solar cells," *Thin Solid Films*, vol. 361-362, pp. 527–532, 2000.

[42] F. Azri, A. Meftah, and M. Amjad, "Electron and hole transport layers optimization by numerical simulation of a perovskite solar cell," *Solar Energy*, vol. 181, pp. 372–378, 2019.

[43] M. Jamil, A. Ali, K. Mahmood et al., "Numerical simulation of perovskite/$Cu_2Zn(Sn_{1-x}\ Ge_x)S_4$ interface to enhance the efficiency by valence band offset engineering," *Journal of Alloys and Compounds*, vol. 821, article 153221, 2020.

[44] J. Chang, L. Jiang, G. Wang, W. Zhao, Y. Huang, and H. Chen, "Lead-free perovskite compounds $CsSn_{1-x}Ge_xI_{3-y}Br_y$ explored for superior visible-light absorption," *Physical Chemistry Chemical Physics*, vol. 23, no. 26, pp. 14449–14456, 2021.

[45] L. Xu, R. Molaei Imenabadi, W. G. Vandenberghe, and J. W. P. Hsu, "Minimizing performance degradation induced by interfacial recombination in perovskite solar cells through tailoring of the transport layer electronic properties," *APL Materials*, vol. 6, no. 3, article 036104, 2018.

[46] Y. Zhao, C. Liang, M. Sun et al., "Effect of doping on the short-circuit current and open-circuit voltage of polymer solar cells," *Journal of Applied Physics*, vol. 116, no. 15, article 154506, 2014.

[47] M. Koopmans, M. A. T. Leiviskä, J. Liu et al., "Electrical conductivity of doped organic semiconductors limited by carrier–carrier interactions," *ACS Applied Materials & Interfaces*, vol. 12, no. 50, pp. 56222–56230, 2020.

[48] A. Stewart, A. D. Julien, D. Regaldo et al., "Shedding light on electronically doped perovskites," *Materials Today Chemistry*, vol. 29, article 101380, 2023.

[49] Y. J. Kim, S. Lee, and M. Kim, "Optimization of perovskite solar cells by varying the acceptor density of the hole-transport layer," *ACS Energy Letters*, vol. 3, no. 10, pp. 2456–2461, 2018.

[50] N. K. Singh and A. Agarwal, "Performance assessment of sustainable highly efficient $CsSn_{0.5}Ge_{0.5}I_3$/$FASnI_3$ based perovskite solar cell: a numerical modelling approach," *Optical Materials*, vol. 139, article 113822, 2023.

[51] P. Roy, Y. Raoui, and A. Khare, "Design and simulation of efficient tin based perovskite solar cells through optimization of selective layers: Theoretical insights," *Optical Materials*, vol. 125, article 112057, 2022.

[52] F. Saeed and H. E. Gelani, "Unravelling the effect of defect density, grain boundary and gradient doping in an efficient lead-free formamidinium perovskite solar cell," *Optical Materials*, vol. 124, article 111952, 2022.

[53] E. Aydin and M. De Bastiani, "Defect and contact passivation for perovskite solar cells," *Advanced Materials*, vol. 31, no. 25, pp. 0935–9648, 2019.

[54] W. Qiu, M. Buffière, G. Brammertz et al., "High efficiency perovskite solar cells using a PCBM/ZnO double electron transport layer and a short air-aging step," *Organic Electronics*, vol. 26, pp. 30–35, 2015.

[55] S. Gyawali, L. K. M. O. Goni, M. S. Chowdhury et al., "Effect of KOH concentration on the properties of ZnO nanoparticles," *Materials Research Express*, vol. 9, no. 5, article 055004, 2022.

[56] N. Pezhooli, J. Rahimi, F. Hasti, and A. Maleki, "Synthesis and evaluation of composite TiO_2@ZnO quantum dots on hybrid nanostructure perovskite solar cell," *Scientific Reports*, vol. 12, no. 1, p. 9885, 2022.

[57] Y. Guo, J. Jiang, S. Zuo et al., "RF sputtered CdS films as independent or buffered electron transport layer for efficient planar perovskite solar cell," *Solar Energy Materials and Solar Cells*, vol. 178, pp. 186–192, 2018.

[58] X. Liu, K. Yan, D. Tan, X. Liang, H. Zhang, and W. Huang, "Solvent engineering improves efficiency of lead-free tin-based hybrid perovskite solar cells beyond 9%," *ACS Energy Letters*, vol. 3, no. 11, pp. 2701–2707, 2018.

[59] Z. Qirong, Z. Bao, H. Yongmao et al., "A study on numerical simulation optimization of perovskite solar cell based on CuI and C60," *Materials Research Express*, vol. 9, no. 3, article 036401, 2022.

[60] F. Baig, Y. H. Khattak, B. Marí, S. Beg, A. Ahmed, and K. Khan, "Efficiency enhancement of $CH_3NH_3SnI_3$ solar cells by device modeling," *Journal of Electronic Materials*, vol. 47, no. 9, pp. 5275–5282, 2018.

[61] T.-B. Song, T. Yokoyama, S. Aramaki, and M. G. Kanatzidis, "Performance enhancement of lead-free tin-based perovskite solar cells with reducing atmosphere-assisted dispersible additive," *ACS Energy Letters*, vol. 2, no. 4, pp. 897–903, 2017.

[62] Y. Gan, X. Bi, and O. Yucheng Liu, "Numerical investigation energy conversion performance of tin-based perovskite solar cells using cell capacitance simulator," *Energies*, vol. 13, no. 22, p. 5907, 2020.

[63] J. Madan, S. Garg, K. Gupta, S. Rana, A. Manocha, and R. Pandey, "Numerical simulation of charge transport layer free perovskite solar cell using metal work function shifted contacts," *Optik*, vol. 202, article 163646, 2020.